

**Magneto-optical properties of (Ga,Mn)As:  
an ab-initio determination**

Alessandro Stroppa

*Faculty of Physics, University of Vienna,  
and Center for Computational Materials Science,  
Universität Wien, Sensengasse 8/12, A-1090 Wien, Austria\**

Silvia Picozzi

*Consiglio Nazionale delle Ricerche, Istituto Nazionale Fisica della Materia (CNR-INFM),  
CASTI Regional Lab., 67010 Coppito (L'Aquila), Italy*

Alessandra Continenza

*CNISM - Dipartimento di Fisica,  
Università degli Studi dell'Aquila,  
67010 Coppito (L'Aquila), Italy*

MiYoung Kim

*BK21 Frontier Physics Research Division,  
Seoul National University, Seoul,  
151-747 (Korea)*

Arthur J. Freeman

*Department of Physics and Astronomy,  
Northwestern University, Evanston,  
IL 60208 (U.S.A.)*

(Dated: February 2, 2008)

## Abstract

The magneto-optical properties of (Ga,Mn)As have been determined within density functional theory using the highly precise full-potential linear augmented plane wave (FLAPW) method. A detailed investigation of the electronic and magnetic properties in connection to the magneto-optic effects is reported. The spectral features of the optical tensor in the 0-10 eV energy range are analyzed in terms of the band structure and density of states and the essential role of the dipole matrix elements is highlighted by means of Brillouin zone *dissection*. Using an explicit representation of the Kerr angle in terms of real and imaginary parts of the tensor components, a careful analysis of the Kerr spectra is also presented. The results of our study can be summarized as follows: i) different types of interband transitions do contribute in shaping the conductivity tensor; ii) the dipole matrix elements are important in obtaining the correct optical spectra; iii) different regions in the irreducible Brillouin zone contribute to the conductivity very differently; iv) a minimum in the  $\text{Re } \sigma_{xx}$  spectra *can* give rise to a large Kerr rotation angle in the same energy region; and v) materials engineering via the *magneto-optical Kerr effect* is possible provided that the electronic structure of the material can be tuned in such a way as to *enhance* the depth of the minima of  $\text{Re } \sigma_{xx}$ .

---

\*Electronic address: alessandro.stroppa@univie.ac.at

## I. INTRODUCTION

The magneto-optical Kerr effect (MOKE), discovered in 1877, [1] consists in the rotation of the polarization plane of linearly polarized light with respect to that of the incident light reflected from a magnetic solid surface. But only very recently has this property become the subject of intense investigations. The reasons are twofold. First, one can exploit this effect to read suitably magnetically stored information using optical means in modern high density data storage technology, erasable video and audio disks (magneto-optical disks).[2, 3, 4, 5, 6] Second, MOKE is now regarded as a powerful probe in many fields of research, such as a microscopy for domain observation,[7] surface magnetism, magnetic interlayer coupling in multilayers, plasma resonance effects in thin layers, and structural and magnetic anisotropies.[8, 9] Magneto-optical measurements are also a valuable tool in the study of the magnetic properties and electronic structure of magnetic materials. Further, it is well known that optical reflection measurements can be used to determine the diagonal elements of the dielectric tensor. However, the reflection spectra of many intermetallic compounds do not show a pronounced fine structure and so the information on the electronic structure obtained through reflection spectra is not very detailed. In contrast, the Kerr effect shows a finer structure and gives important insights into the properties of transition-metal and rare-earth compounds.[10, 11, 12]

In the last ten years, transition metal doped semiconductors have attracted considerable attention in the field of *spintronics*,[13, 14, 15] where  $\text{Ga}_{1-x}\text{Mn}_x\text{As}$  is by far the most studied material suitable for semiconductor-based spintronic devices.[16, 17, 18] Interestingly, the giant magneto-optical effects observed in some of these systems are especially attractive for optical applications.[19, 20, 21] For instance, optical isolators based on magnetic semiconductors might be ideal components for high speed optical communication systems.[22] Furthermore, magneto-optical measurements have been playing an important role in clarifying the exchange interaction and the electronic structure of these ferromagnetic semiconductors, as they provide very detailed information on the influence of broken time-reversal symmetry in itinerant electron quasi-particle states.[22]

Despite the increasing role of magnetic semiconductors over the last years, and the extensive studies available on their electronic and magnetic properties,[23, 24, 25, 26, 27, 28, 29] only very recently have *ab-initio* calculations of their magneto-optical properties been

performed.[30, 31, 32] Weng *et al.* studied the electronic structure and polar magneto-optical Kerr effect of transition metal chalcogenides, such as CrSe, CrTe, and VTe in zinc-blende and wurtzite structures, by full-potential density-functional calculations[31], while in a following paper Weng *et al.* analyzed the magneto-optical response of  $\text{Zn}_{1-x}\text{Cr}_x\text{Te}$  ordered alloys. In Ref. 30, some of us investigated the magneto-optical properties of  $\text{Ga}_{1-x}\text{Mn}_x\text{As}$  with highly precise first-principles density-functional FLAPW calculations in order to perform an accurate comparison with experiments, focusing on the effect of Mn concentration and of the occupied sites.

The purpose of the present work is to go beyond the analysis presented in Ref. 30, by performing an extensive study focused on the optical conductivity tensor as well as on the Kerr spectra. Here we mainly focus on (Ga,Mn)As ferromagnetic semiconductors in the high concentration limit by considering a 25% concentration of Mn substituting for Ga. Although this can be considered as a rather unrealistic case due to the low solubility of Mn in the host GaAs crystal, important aspects of the interplay between the underlying electronic structure and the MO Kerr effect (MOKE) can be gained and then extended to the low-concentration limit. We therefore studied the optical conductivity in connection with the electronic structure. As analysis tools, we considered the density of states (DOS) and band structure in order to elucidate the origin of the features of the optical spectra in terms of electronic transitions. The origin of these features are further investigated by performing an analysis of the electronic transitions throughout the Brillouin zone (**k**-space dissection). In this way, the contributions coming from the different regions of the Brillouin zone can be separated out and the role of the dipole matrix elements can be quantitatively analyzed. Finally, in order to compare our results with available experiments, we considered a more dilute case, namely  $x=6.25\%$ .

After the analysis of the optical properties, we turn our attention to the study of the Kerr spectra. Our approach is based on a *real* representation of the Kerr angle. We show, using such a representation, that useful analytical relations can be derived and can be used to gain insights into the microscopic quantities that determine the magnitude and frequency position of the main features in the Kerr rotation spectrum.

The work is organized as follows: in the next section, we briefly describe the theoretical methods and provide computational details; in Sect. III, we review the electronic and magnetic properties of  $\text{Ga}_{0.75}\text{Mn}_{0.25}\text{As}$ ; Sect. IV is devoted to the analysis of the optical con-

ductivity tensor in terms of the band structure; in Sect. V we perform a full  $\vec{k}$ -space analysis in order to highlight the role of dipole matrix elements in shaping the optical spectra; in Sect. VI, we analyze in detail the Kerr spectra; finally, in Sect. VII, we draw our conclusions.

## II. THEORETICAL FRAMEWORK AND COMPUTATIONAL DETAILS

In this work, the Kohn-Sham equations are solved self-consistently, using the full-potential linearized augmented plane wave (FLAPW) method.[33] We used the local spin density approximation (LSDA) for the exchange-correlation functional, with the parametrization of Hedin-Lundqvist.[34] The spin-orbit coupling (SOC) is essential to obtain the orbital magnetic moment as well as the magneto-optical effects:[35, 36] in the evaluation of the optical conductivity, the spin orbit effect is neglected in the self-consistent iterations but is included in a second variational step.

The optical conductivity tensor is calculated according to the Kubo formula in the linear response theory:[37, 38, 39]

$$\sigma_{\alpha,\beta}(\omega) = \frac{Ve^2}{8\pi^2\hbar m^2\omega} \sum_{n,n'} \int d^3\vec{k} <\vec{k}n|p_\alpha|\vec{k}n'> <\vec{k}n'|p_\beta|\vec{k}n> f_{\vec{k}n}(1 - f_{\vec{k}n'})\delta(\epsilon_{\vec{k}n'} - \epsilon_{\vec{k}n} - \hbar\omega) \quad (1)$$

where  $\alpha, \beta=1, 2, 3$ ;  $p_\alpha$  are components of the momentum operator,  $f_{\vec{k}n}$  is the Fermi distribution function ensuring that only transitions from occupied to unoccupied states are considered;  $|\vec{k}n>$  is the crystal wave function, corresponding to the Kohn-Sham eigenvalue  $\epsilon_{\vec{k}n}$  with crystal momentum  $\vec{k}$ ; and the delta function warrants total energy conservation. The above formula considers infinite lifetime of excited Bloch electronic states. In order to take into account finite lifetime effects, we broadened the optical spectra by fixing the interband relaxation time for excited states to 0.3 eV.

Equation 1 contains a double sum over all energy bands, which naturally splits into the so-called interband contributions, *i.e.*,  $n \neq n'$ , and the intraband contributions,  $n = n'$ , that is:

$$\sigma_{\alpha,\beta} = \sigma_{\alpha,\beta}^{inter}(\omega) + \sigma_{\alpha,\beta}^{intra}(\omega) \quad (2)$$

For the diagonal tensor components, both terms are important and should be considered simultaneously. For metals (or half-metals), the intraband contribution to the diagonal

component of  $\sigma$  is usually described by the phenomenological expression according to the Drude-Sommerfeld model:[40, 41]

$$\sigma_D(\omega) = \frac{\omega_P^2}{4\pi[(\frac{1}{\tau_1}) - i\omega]} \quad (3)$$

Within the Drude theory framework, the complex conductivity is fully characterized by two parameters: the plasma frequency  $\omega_P$  and the relaxation rate  $\gamma_1 = 1/\tau_1$ . The intraband relaxation time,  $\tau_1$ , characterizes the scattering of charge carriers, which depends on the amount of defects and therefore varies from sample to sample. Here we choose a fixed value of 0.7 eV for  $\gamma_1$  in all our simulations. It is worth noting that this value does not affect our discussion below, and, in any case, variations of its value between 0.2 and 0.7 eV, which include the usual variability range for  $\gamma_1$ , [42] lead to a negligible effect on the optical conductivity for energy values larger than 1 eV. The unscreened plasma frequency is obtained integrating over the Fermi surface:

$$\omega_{P,ii}^2 = \frac{8\pi e^2}{V} \sum_{\mathbf{k}n,s} | \langle \mathbf{k}ns | p_i | \mathbf{k}ns \rangle |^2 \delta(\varepsilon_{\mathbf{k}n} - \varepsilon_F) \quad (4)$$

where  $V$  is the volume of the primitive cell,  $\varepsilon_F$  the Fermi energy,  $e$  the electron charge and  $s$  is the spin. The calculated value of  $\omega_P$  is  $2.42 \times 10^{14}$  Hz (2.75 eV). The intraband contribution to the off-diagonal optical conductivity is very small and is usually neglected in the case of magnetically ordered materials.[43]

In the present work, we consider the Kerr effect in the so-called polar geometry, where the magnetization vector is oriented perpendicular to the reflective surface and parallel to the plane of incidence. In such a case, the Kerr rotation angle  $\theta_k(\omega)$  and its ellipticity  $\eta_k(\omega)$  can be obtained from the conductivity tensor as:

$$\theta_k(\omega) + i\eta_k(\omega) = - \frac{\sigma_{xy}(\omega)}{\sigma_{xx}(\omega) \sqrt{1 + i(4\pi/\omega)\sigma_{xx}(\omega)}} \quad (5)$$

Our study is based on the supercell approach where one of the Ga atoms in an 8-atom cell of zinc-blende GaAs is replaced by a Mn atom, thus simulating an ordered alloy with an x=25% Mn concentration. The lattice parameter is chosen equal to the experimental lattice parameter of GaAs (5.65 Å). For larger unit-cells, *i.e.* x = 6.25 %, we refer to the work of Picozzi *et al.*, [30] where the pertinent computational and structural details are given.

As far as the other technical details are concerned, we used a wave-vector cutoff of the basis set equal to  $K_{max}=3.5$  a.u. and an angular momentum expansion up to  $l_{max} = 8$  for both the potential and charge density. The muffin-tin radius,  $R_{MT}$ , for Mn, Ga and As were chosen equal to 2.1, 2.3, and 2.1 a.u., respectively. The relaxed internal atomic positions were obtained by total-energy and atomic-force minimization using the Hellmann-Feynman theorem[44] with residual forces below 0.015 eV/Å. The sampling of the irreducible wedge of the Brillouin zone (IBZ) was performed using the special  $k$ -point method.[45] In order to speed up the convergence of the sampling, each eigenvalue is smeared with a Gaussian function of width 0.03 eV. The ground-state electronic structure is calculated using a  $4\times 4\times 4$  cubic mesh. We checked that these computational parameters are accurate enough to obtain total energies and magnetic moments within 10-15 meV/Mn and  $0.01 \mu_B$  (keeping the muffin-tin radii fixed), respectively. On the other hand, in order to accurately compute the optical conductivity, the  $k$  integration must be carefully taken care of. We investigated its accuracy by varying the number of  $k$  points up to a (10,10,10) shell (35  $k$ -points in the IBZ): we get the Kerr rotation angle and ellipticity within a few hundredths of a degree already using a (4,4,4) shell.

### III. ELECTRONIC AND MAGNETIC PROPERTIES

Before discussing the magneto-optical (MO) properties, we consider in some detail the electronic structure and the magnetic properties of  $\text{Ga}_{0.75}\text{Mn}_{0.25}\text{As}$ . Although shown and discussed in several previous publications,[46, 47, 48, 49, 50, 51, 52, 53] we show them in Fig. 1 and Fig. 2, as it is fundamental to have in mind a clear picture of the electronic and magnetic properties of the compound considered. This is needed in order to consistently follow the discussion of the optical conductivity tensor (see below), which is the main issue of the present work. In particular, in Fig. 1 we show the spin polarized total density of states (DOS) and the site angular momentum-projected DOS (PDOS) for Mn and nearest- and next-nearest-neighboring atoms, that is As and Ga atoms, respectively. In Fig. 2, we show the spin-polarized band structure (not including spin-orbit coupling), along the  $\Gamma$ -X-M- $\Gamma$ -R-M symmetry directions, for the majority (left) and minority (right) bands. Numbers in round brackets label groups of bands (eventually degenerate) at the  $\Gamma$  point. Vertical

dashed lines denote the electronic transitions giving rise to spectral features in  $\text{Re } \sigma_{xx}$  (see next Section), and in the following, we discuss both Figs. 1 and 2. The total DOS (see Fig.1, topmost panel) shows the *nearly* half-metallic (n-HM) nature of the electronic ground state: the majority bands cross the Fermi level (set to zero) whereas a net gap opens in the minority bands with the Fermi level cutting the minority conduction band near  $\Gamma$ .

The total DOS curve is composed of several characteristic structures whose origin can be easily recognized by looking at the partial (P)DOS curves. In the following, we only consider the upper part of the valence band (above the ionicity gap, that is above  $-7.5$  eV) and the lower part of the conduction band (up to  $\sim 5$  eV) which define the energy window relevant for the optical transitions we are interested in. The peak centered at  $-6$  eV in the DOS curve (for both spin components) is dominated by the energetically low-lying Ga-*s* states, and corresponds to the lowest lying bands in Fig. 2, [(1) and (1a)], which are rather (surprisingly) well dispersed along  $\Gamma$ -X-M- $\Gamma$ , and almost flat in the  $\Gamma$ -R-M direction. As the energy increases, there is a peak at  $-5.0$  ( $-4.6$ ) eV in the majority (minority) component, which mainly derives from *s*-Mn; it corresponds to the next low-lying band shown in Fig. 2, [(2) and (2a)], which is degenerate with the lowest band [(1) and (1a)] at *R*.

A broader structure in the total DOS extends from about  $-4.0$  eV up to  $E_F$  (majority component) and up to about  $-1.0$  eV (minority component). Let us consider the majority component. The sharp peak at  $-3.0$  eV originates from Mn-*d* orbitals and corresponds to the group of bands in Fig. 2 [(3)]; these bands are degenerate at  $\Gamma$  and are split into three bands along  $\Gamma$ -M and into two bands along  $\Gamma$ -R. Inspection of the eigenvalue decomposition shows that these states have  $t_2$  symmetry at  $\Gamma$  and thus they hybridize with anion *p* states (see the corresponding PDOS curve in Fig. 1). In general, the higher energy bands [groups (4) and (5) in Fig. 2] mostly derive from hybridization between Mn-*d* and As-*p* states, as well as the bands [(6) and (7)] around  $E_F$ . The Mn-*s* states contribute little to the defect bands since they obviously lie lower in energy than the Mn-*d* and -*p* states. One also recognizes the intra-atomic hybridization (among states of the same atom) occurring for Mn-*p* and -*d* states: the corresponding DOS curves overlap in a wide energy range. Higher bands [(8)] are mostly derived from cation and anion states. For the minority component, the valence bands, [(3a), (4a) and (5a) in Fig. 2], are mostly dominated by As-*p* states. The Mn-*d* states are pushed upward in energy above  $E_F$ , due to exchange splitting: these states are almost unoccupied and remain fairly narrow in energy above the gap. The conduction bands



[(6a), (7a) and (8a)] are composed of Mn-*d* and -*p* states just above  $E_F$ , while higher bands [(9a)] mainly by Ga-*s* and As-*p* states. The same Mn-*p*, -*d* intra-atomic mixing is found in the minority component above  $E_F$  (the Mn-*p* and -*d* DOS are localized in the same energy range).

## IV. OPTICAL CONDUCTIVITY

### A. General considerations

In Fig. 3, we show the (a) real (left) and (b) imaginary (right) parts of the diagonal (top) and off-diagonal (bottom) components of the conductivity, in the range 0-10 eV. For simplicity, we did not include the Drude term in the conductivity curves shown. In the real part of the diagonal component ( $\text{Re } \sigma_{xx}$ ), we highlight some features with vertical lines, which will be discussed in closer detail later.

The  $\text{Re } \sigma_{xx}$  curve has a quite broad peak at around 3.8 eV whereas the  $\text{Im } \sigma_{xx}$  curve shows a deep minimum in the low energy range (around 2.3 eV) and a shoulder above 6.8 eV. The  $\text{Re } \sigma_{xy}$  curve shows small amplitude oscillations in the energy range 0–4 eV; a deep minimum is found at  $\sim 5$  eV, and a maximum follows at  $\sim 6.8$  eV followed again by oscillations with small amplitude. The imaginary component,  $\text{Im } \sigma_{xy}$ , has similar characteristics in the low and high energy range (small amplitude oscillations), but a maximum develops at  $\sim 4.6$  eV and a minimum follows at  $\sim 6.4$  eV.

The absorptive part of the off-diagonal optical conductivity,  $\text{Im } \sigma_{xy}$ , has a direct physical interpretation. It is proportional to the difference in absorption rate of the left and right circularly polarized (LCP and RCP) light, and its sign is directly related to the spin polarization of the states responsible for the interband transitions producing the structures in the spectrum.[54] The peak in  $\text{Im } \sigma_{xy}$  around 4.6 eV suggests that interband transitions related to LCP light should be stronger in this energy region. On the other hand, around 6.4 eV,  $\text{Im } \sigma_{xy}$  shows a deep minimum value, indicating the dominance of interband transitions related to RCP. Finally,  $\text{Im } \sigma_{xy}$  is negligible when the absorption coefficient for RCP is equal to that of LCP - i.e., in the lowest and highest parts of the spectrum.

## B. Analysis in terms of band structure

Since  $\text{Re } \sigma_{xx}$  is directly related to the density of states and transition probabilities,[54] we investigate the calculated energy band structure in order to analyze the details of the spectra. It has been known for quite some time that both the spin-orbit (SO) interaction and the exchange splitting are needed to produce a non-zero Kerr effect.[35, 55, 56] Therefore, a proper analysis should be performed considering the band structure with spin-orbit (SO) included. However, we remark that the calculated band structure with SO (not shown here) is quite similar to that formed by the superposition of the majority and minority spin bands (without SO). This corresponds to a spin-orbit coupling interaction that is small compared to the exchange splitting, so we can qualitatively consider the former as a perturbation to the latter:[57] this allows us to restrict our discussion to the usual spin-polarized band structure, thus neglecting the mixing of majority and minority spin components. In this way, a decomposition with respect to each separate spin channel (spin up, down) can be done; this decomposition is almost uniquely determined if the spin-orbit coupling is weak. Inspection of the eigenvalue decomposition at  $\Gamma$  shows that the exchange-splitting of As- $p$  and Mn- $d_{eg}$  states are  $\sim 0.03$  and  $2.5$  eV, respectively, whereas the spin-orbit splitting is  $\sim 0.02$  and  $0.002$  eV, respectively. In this case, the main effect of the SO interaction is just to remove some accidental and systematic degeneracies[58, 59, 60].

In Fig. 2, we can recognize three different contributions coming from the band structure which build up the optical spectra: (a) close parallel bands crossing  $E_F$ ; (b) bands which are degenerate (or almost degenerate) at one point and then separate out, moving below and/or above  $E_F$ ; and (c) occupied/unoccupied bands which are almost parallel in a significant part of the Brillouin zone.[61] The first type does contribute to the conductivity in the low energy range and gives rise to bumps of interband transitions; the second type gives rise to an almost constant amount of interband transitions with a distinct onset energy; the third type gives rise to peaks at higher energies. In the following, we refer to *bands* although a more appropriate discussion should be done in terms of *constant eigenvalue surfaces* in reciprocal space.[62] However, the purpose of this section is to analyze on a qualitative level the origin of the different structures in  $\text{Re } \sigma_{xx}$ . For this purpose, we highlight the relevant electronic transitions (see Fig. 2) that give rise to the spectral features in the  $\text{Re } \sigma_{xx}$  curve at 0.4, 1.1, 2.8 and 3.8 eV (see Fig. 3), respectively.

$\text{Re } \sigma_{xx}$  is non-negligible already at rather low energies (as low as 0.5 eV, see Fig. 3). As can be seen from Fig. 2, interband transitions are available at this energy due to bands which are degenerate at some  $\vec{k}$  points at energies slightly below (or above)  $E_F$  and then separate out, moving above  $E_F$  [type (b) transitions]. For example, in the minority component, the main contribution in this energy range comes from the two bands [(6a)] below  $E_F$ , which are degenerate at  $\Gamma$  and split along  $\Gamma$ -X and  $\Gamma$ -M. Incidentally, we note that the same bands are responsible for the n-HM character of the (Ga,Mn)As compound. At very low energy, the bands along  $\Gamma$ -M do contribute to the conductivity, whereas those along  $\Gamma$ -X do so at higher energies.

Consider in detail the minority bands along  $\Gamma$ -X with energies just below  $E_F$  [bands (6a) at  $\Gamma$ , see Fig. 2]. A careful inspection of the eigenvalue decomposition into atomic-site-projected wave functions shows that these bands have a prevalent  $d$  character but with a non-negligible contribution from anion  $p$  as well as  $s$  cation states. Moving away from the zone center, the  $d$  as well as  $p$  contributions increase in the higher energies of these bands, while the  $s$  contribution decreases; the opposite occurs for the lower band. The  $d - p$  and  $s - p$  mixing is crucial for the onset of the dipole transitions among these states at very low excitation energies which otherwise would be forbidden by selection rules. Moving away from  $\Gamma$ , their energy separation increases, as is typical for type (b); as the lower band crosses  $E_F$ , the interband transitions stop contributing at an excitation energy around 0.40 eV. This corresponds to the first flat region in  $\text{Re } \sigma_{xx}$  starting around 0.40 eV. Other electronic transitions at 0.40 eV are shown in Fig. 2 with lines near the M point in the spin-up bands.

Upon further increase of the excitation energy, additional type (b) structures start contributing, like the majority group of bands [(7)] above  $E_F$  and degenerate at R which split along R- $\Gamma$  and R-M. In particular, along R- $\Gamma$ , one band remains above  $E_F$ , while the other goes below. This causes an increase of  $\text{Re } \sigma_{xx}$ , at energies lower than 1.0 eV. In this energy range, type (a) bands also contribute, like the almost parallel majority bands which cross  $E_F$  along  $\Gamma$ -M, and those crossing  $E_F$  along  $\Gamma$ -X [all of them deriving from bands (6) and (7)].

As the photon energy reaches  $\sim 1.1$  eV, several transitions are activated, accounting for the bump in the conductivity. The transitions at 1.1 eV are shown with blue (dotted) lines in Fig. 2. In the majority (minority) component, they are mainly localized near the R ( $\Gamma$ ) point [mostly type (c) transitions].

At  $\sim 2.8$  eV, we have a bump in the  $\text{Re } \sigma_{xx}$  (see Fig. 3). First, let's consider the minority component. The almost dispersionless occupied band around  $-1.0$  eV [(5a)] is coupled to the group of bands around  $1.5$  eV [(8a)]. These are type (c) transitions and they give rise to the bump in  $\text{Re } \sigma_{xx}$  around  $2.8$  eV. The transitions which match the energy of  $2.8$  eV are shown by red (dashed) lines in Fig. 2. In the majority component there is also a contribution coming from the group of bands (5) and (7). As the photon energy increases,  $\text{Re } \sigma_{xx}$  reaches its maximum value, at around  $3.8$  eV. There are several contributions to this peak: they involve degenerate minority bands at high symmetry points, like the groups of bands at  $\Gamma$  centered at  $-2.5$  eV [(4a)] and  $1.5$  eV [(8a)] and at R with energies  $\sim -2.0$  eV and  $2.0$  eV, respectively. In the majority components, more type (c) transitions contribute to the maximum of  $\text{Re } \sigma_{xx}$ . They mainly involve groups of degenerate bands at  $\Gamma$  (occupied/unoccupied) which split along  $\Gamma$ -M: they are not flat along this symmetry line but are almost parallel near  $\Gamma$ . For instance, the highest of this group of bands [(5)] split along  $\Gamma$ -M couples with the lowest of the group of bands [(8)].

As the photon energy increases, the lowest majority and minority energy bands between  $-5$  and  $-7$  eV below  $E_F$  come into play. The dispersion of the occupied as well as the unoccupied bands involved in the transitions increases, and this correlates with the conductivity decrease.

It can be useful to consider the role of the electrons with spin up and spin down in shaping the spectra of  $\text{Re } \sigma_{xx}$ . Again, this can be done on a qualitative level only. In fact, the dipole matrix elements enter quadratically in the calculation of the conductivity (see Eq. 1) and *interference effects* can be lost by separating the spin-up or spin-down contributions to the conductivity. Indeed, from Eq. 1, we have, for  $\alpha=\beta=x$  and neglecting the  $\vec{k}$  index:

$$\langle n|p_x|n' \rangle \langle n'|p_x|n \rangle = |\langle n|p_x|n' \rangle|^2 \quad (6)$$

where  $n$  includes the spin indices. Expressing the spin indices, and neglecting spin-flip transitions[63, 64] we have:

$$|\langle n|p_x|n' \rangle|^2 = \left| \sum_{ss'} p_{x,nn'}^{ss'} \right|^2 = |p_{x,nn'}^{\uparrow\uparrow}|^2 + |p_{x,nn'}^{\downarrow\downarrow}|^2 + 2\text{Re}(p_{x,nn'}^{\uparrow\uparrow} p_{x,nn'}^{\downarrow\downarrow*}) \quad (7)$$

In Fig. 4, we show the two spin contributions to  $\text{Re } \sigma_{xx}$ , *i.e.* neglecting the last term in Eq. 7, in the range 0-10 eV. Incidentally, we note that the *sum* of the two separate contributions (which does not include the interference effects coming from the last term in Eq. 7), not shown in Fig. 4, differs in some fine details from the curve shown in Fig. 3 (which naturally includes the interference effects). This confirms a posteriori that the loss of interference effects due to neglecting the last term in Eq. 7 introduces a negligible error and allows us to treat the two spin contributions to the conductivity separately. The two curves are qualitatively similar, and they clearly show the origin of the bump at 2.8 eV and the maximum at 3.8 eV: the former is mainly due to transitions involving minority while the latter the majority spin bands. From Fig. 2 one could conclude that both the features at 2.8 and 3.8 eV arise from minority spin band transitions: this is not exactly true due to the role of the dipole matrix elements.

In the same Fig. 4, we also show the joint density of states (JDOS), which can be derived from Eq. 1 by replacing the matrix elements with a constant factor set to 1 in our case.[54] This quantity clearly highlights the role of the dipole matrix elements: as a matter of fact, the JDOS does not show any relevant feature in the spectra stressing that the spectral features observed occur primarily due to the very large matrix elements rather than to a large joint density of states effect. On the same basis, the large shoulder above 6 eV in the JDOS does not produce any peak in the conductivity spectra due to the small matrix elements.

### C. Comparison with experiments

Finally, we compare our calculations with some experimental results. For this purpose, we consider a lower concentration  $x = 6.25\%$  (1 Mn in a 32-atom cell) that is closer to available experiments.[65, 66, 67] In Fig. 5 (a) we show the calculated real component of the diagonal optical conductivity,  $\text{Re } \sigma_{xx}$ , as a function of the photon frequency, compared with spectra obtained from experiments and model calculations [68] for  $\text{Ga}_{0.95}\text{Mn}_{0.05}\text{As}$  (at hole concentration  $p \sim 0.8 \text{ nm}^{-3}$ ), in the [0.01-2] eV energy range. In this interval, our calculated conductivity is of the order of  $1\text{-}2 \cdot 10^3 \text{ (ohm}\cdot\text{cm)}^{-1}$ , *i.e.*, remarkably larger (almost by an order of magnitude) than the experimental values[65] but of the same order of magnitude as the results of model calculations.[68] The disagreement with experiments may be fully explained

in terms of the suggested values of carrier concentration in the experimental samples:  $p \sim 0.35 \text{ nm}^{-3}$  for a Mn concentration on the order of  $\sim 6\%$ , with a degree of compensation on the order of 70-80%.

In our systems, a pretty naive evaluation of the hole concentration can be obtained by supposing that each Mn - with a nominal valence of +2 - substituting a Ga atom gives rise to a hole; therefore, 1 Mn atom in a 32 atom cell produces a hole concentration of  $1.38 \text{ nm}^{-3}$ . It has been shown[68] that the hole concentration has a relevant influence on the optical conductivity: for example, at very low energies ( $< 0.01 \text{ eV}$ )  $\sigma_{xx}$  ranged [68] from  $\sim 1.5 \times 10^2$  to  $\sim 3.5 \times 10^3 (\text{ohm}\cdot\text{cm})^{-1}$  for hole concentrations varying from  $p \sim 0.03$  to  $0.80 \text{ nm}^{-3}$ . These values are very consistent with the range in which our conductivity falls. Looking at the trend as a function of energy, our  $\sigma_{xx}$  spectrum is generally featureless, with the exception of the minimum at 800-1000 meV - in remarkably close agreement with experimental as well as model calculation results.[68] In the inset, we show the effect of including the Drude contribution to the spectra in an extended energy range: as expected, only in the low energy range ( $< \sim 1.5 \text{ eV}$ ) does the Drude term significantly contribute to the total spectra. In particular, the above mentioned minimum is present in both total and interband-only terms, but it is much more enhanced upon inclusion of the Drude term, therefore improving the agreement with experiment.

The real and imaginary parts of the dielectric constant,  $\epsilon_{xx}$ [69], are shown in Fig. 5 (b) and (c), respectively, and compared with experimental ellipsometry measurements.[66] The agreement is rather good, as far as the overall features are concerned. However, there is a sizeable discrepancy in the energy position of peaks and valleys. This has probably to be ascribed to the neglect of self-energy corrections or to the incorrect treatment of correlation effects, resulting in an only partial description of the underlying electronic structure. In order to improve the agreement with experiment, we used the so-called  $\lambda$ -fitting procedure, suggested by Rhee *et al.* (see Ref. [70] for details), which is an oversimplified approach to include a rescaling in the excitation energy spectrum, avoiding the complicated task of properly evaluating self-energy effects. Using a value of  $\lambda \sim -0.1 \text{ eV}$ , both the real and imaginary spectra were reasonably reproduced.

## V. $\vec{k}$ SPACE DISSECTION

In this section, we study the origin of the spectral features of  $\text{Re } \sigma_{xx}$ . The qualitative analysis discussed in the previous section is based on the band structure which highlights only transitions involving electronic states at symmetry points or lines in the irreducible BZ (IBZ). Here we examine the spectrum in further detail, taking into account the contributions coming from the full IBZ. Thus, we sample the BZ with an  $8 \times 8 \times 8$  cubic shell and evaluate the matrix elements in Eq. 1 in a small energy window ( $\delta_e = 0.2$  eV) centered around the spectral feature of interest. For each  $\mathbf{k}$ -point, the contribution to the conductivity ( $\sigma_{\mathbf{k}}^{\delta_e}$ ) was evaluated calculating the dipole matrix elements between the initial and final states contributing within the selected energy window. Finally, the  $\sigma_{\mathbf{k}}^{\delta_e}$  have been normalized to unity,  $\tilde{\sigma}_{\mathbf{k}}^{\delta_e}$ . At each  $\mathbf{k}$ -point, the  $\tilde{\sigma}_{\mathbf{k}}^{\delta_e}$  is graphically represented by an arrow whose length is proportional to its magnitude. The results are shown in Fig. 6.

From this plot, one can easily visualize the region of  $\mathbf{k}$ -space contributing to the features in the conductivity spectra. We focus on the maximum of  $\text{Re } \sigma_{xx}$ , at 3.8 eV. Figure 6 shows the origin of all interband transitions in the range 3.6-4.0 eV, contributing to the maximum of  $\text{Re } \sigma_{xx}$ . First, we note that different regions in the IBZ contribute to the conductivity very differently: the largest contributions come from the region around the R point, and the strength of the contributions decreases upon moving towards M and X. The  $\mathbf{k}$ -points where large interband transitions occur belong to a line parallel to M-R, suggesting that these are transitions between bands or band pairs which are very flat throughout much of this symmetry line or transitions with very large dipole matrix elements. The contributions from planes parallel to R-X-M rapidly decrease in amplitude and become negligible for  $\mathbf{k}$ -points close to  $\Gamma$ . From this, it is clear that the most active region in the IBZ in shaping the maximum of  $\text{Re } \sigma_{xx}$  is the region parallel to the R-X-M plane, near the edge of IBZ.

## VI. MAGNETO-OPTICAL PROPERTIES

We now turn our attention to the Kerr spectra. Equation 5 suggests that the Kerr angle could be enhanced by a large magneto-optical component ( $\sigma_{xy}$ ) and a small optical component ( $\sigma_{xx}$ ). To investigate the Kerr spectra on a qualitative level, one can consider the separate contributions of the numerator  $\sigma_{xy}(\omega)$  and the denominator  $D(\omega) =$

$\sigma_{xx}(\omega)\sqrt{1 + \frac{4\pi}{\omega}\sigma_{xx}(\omega)}$ . The corresponding features in the imaginary part of the spectra are then correlated to those observed in the Kerr spectra. This analysis has been done in Ref. 30 by some of us, to which we refer the reader for further details. Incidentally, we note that our spectrum (presented in Fig. 7, see below) is quite similar to those presented in Ref. [30] for  $x = 6.25\%$  and  $x = 12.5\%$ . We can conclude that the main features of the Kerr spectra of (Ga,Mn)As do not depend to a great extent on the Mn concentration, at least for the cases considered: this further validates our choice to focus on the high concentration limit in this study.

As pointed out by Schoenes and Reim, [71], the form given by Eq. 5 of the Kerr rotation is *not* the most suitable to discuss due to the complex denominator. Indeed, it is possible to express the real part of the left hand side of Eq. 5 (that is the Kerr angle) in terms of the real part of the *complex fraction* appearing in the right hand side of Eq. 5. In this way, one ends up with a *real fraction* where the denominator ("optical component") depends *only* on  $\text{Re } \sigma_{xx}$  and  $\text{Im } \sigma_{xx}$  and the numerator ("magneto-optical component") depends on *both* the real and imaginary parts of  $\sigma_{xx}$  and  $\sigma_{xy}$  (see the Appendix):

$$\theta_K = -\frac{A(\omega)p(\omega) + B(\omega)q(\omega)}{D_0(\omega)D_1(\omega)} \quad (8)$$

with  $A = R\sigma_{xy}R\sigma_{xx} - I\sigma_{xy}I\sigma_{xx}$  and  $B = I\sigma_{xy}R\sigma_{xx} - R\sigma_{xy}I\sigma_{xx}$ . (Here, R and I refer to Real and Imaginary part, respectively). For the definitions of  $p$ ,  $q$ ,  $D_0$ , and  $D_1$  we refer to the Appendix. We further define  $N_1 = -A(\omega)p(\omega)$ ,  $N_2 = -B(\omega)q(\omega)$ ,  $N=N_1+N_2$  and  $D=D_0D_1$  so that  $\theta_K = N/D$ . We will show that this decomposition can be useful to study the correlations between features of the Kerr spectra and electronic structure.

In Fig. 7, we show: ellipticity ( $\varepsilon_K$ ), and Kerr angle ( $\theta_K$ , in decimal degree), in panel (a);  $N_1$ ,  $N_2$  and  $N$  in panel (b);  $D_0$ ,  $D_0^{-1}$ , and  $\text{Re } \sigma_{xx}$  (the spectrum has been rescaled in such a way that  $\text{Re } \sigma_{xx}$  and  $D_0$  have the same maximum value) in panel (c);  $D_1$ , and  $D_1^{-1}$  in panel (d); and finally  $D$ ,  $\text{Re } \sigma_{xx}$  (the spectrum has again been rescaled in such a way that  $\text{Re } \sigma_{xx}$  and  $D$  have the same maximum value), and  $D^{-1}$ , in panel (e). The notation  $D_{...}^{-1}$  means  $1/D_{...}$  (reciprocal function). All the quantities, except the Kerr angle, are in arbitrary units.

Let us focus on the Kerr ellipticity and rotation [panel (a)]. Clearly, they are related: when the Kerr ellipticity crosses the zero line, a peak appears in the Kerr rotation spectra due to the Kramers-Kronig relations.[31] It is interesting to note that the theoretical ellipticity



curve crosses/touches the zero axis a number of times, hence suggesting that the incident linearly polarized light, at these frequencies, would stay as linearly polarized only. The Kerr rotation is characterized by several spikes as well as sign reversals in the whole energy window. In particular, there is a first magneto-optical resonance ( $0.56^\circ$ ) at  $\hbar\omega \sim 0.2$  eV and other main peaks are located at  $\sim 1, 2$  and  $6$  eV. The arrows in the Kerr spectra mark the main features (positive and negative). From Fig. 7 [panels (a),(b)], we see that the shape of the Kerr spectra is mainly determined by  $N_1$  in the low energy range (0-3 eV), by both  $N_1$  and  $N_2$  in the medium energy range (3-7 eV), and by  $N_2$  in the high energy range (7-10 eV). Very interestingly, the overall spectral trend of the Kerr angle, such as the peaks and sign reversal positions, are very close to that of the numerator  $N(\omega)$  [panel (b)], and only the relative heights of the spikes are different. As expected, the zero of  $N(\omega)$  fixes the zero in the Kerr spectra. We can draw the first conclusion:  $N(\omega)$  determines the overall trend of the Kerr spectra, and, in particular, the presence of maxima and minima. We also stress that the analytic form of the numerator of the Kerr angle (see Eq. 8 and the Appendix) *entangles* in a rather complicated way *all* the real and imaginary components of the conductivity tensor: there is no simple guideline to link the trend of a part of the Kerr spectra to the spectral trend of a specific (real or imaginary) tensor component in the same energy range.

We now focus on the denominator  $D^{-1}$ . First we write  $\theta_K = N(\omega)D^{-1}(\omega)$ , so that  $D^{-1}$  plays the role of an *enhancement* factor. It is evident that both  $D_0$  and  $D_1$  are positive definite, that is they never cross the zero line: the *enhancement* factor does not have any "resonant" behavior. In Fig. 7 panel (c), we can see that, remarkably, the spectral trend of  $D_0$  is very *similar* to  $\text{Re } \sigma_{xx}$ . We might therefore infer that  $D_0^{-1}$  has large values whenever  $\text{Re } \sigma_{xx}$  has its smallest ones. In our case, this happens when the photon energy approaches  $\sim 0$  eV. On the other hand,  $D_1$  [panel (d)] does not show any remarkable features, apart from the maximum at very low energy. Considering that the reciprocal function  $D_0^{-1}$  [panel (c)] exhibits a maximum at  $\sim 0$  eV and strongly decreases with increasing energy,  $D_1^{-1}$  has a minimum at  $\sim 0$  eV and monotonically increases with energy.  $D_1^{-1}$  is also featureless, in almost the whole energy window. From panel (e), we see that  $D^{-1}$  has a large peak around  $\sim 0.5$  eV, then decreases very fast to an almost constant value, and slowly increases at energies larger than  $\sim 5$  eV. Clearly, the shoulder of  $D^{-1}$  at low energy comes from the behavior of  $D_0^{-1}$  and  $D_1^{-1}$  in the same energy range, whereas the increase of  $D^{-1}$  at high energy is mainly

due to the behavior of  $D_1^{-1}$  in the corresponding energy range.

These results clearly explain the *origin* of the Kerr spike ( $0.56^\circ$ ) at  $\sim 0.2$  eV. The numerator determines the existence and location of the spikes: whether they give rise to a strong Kerr angle follows entirely from the *enhancement* factor,  $D^{-1}$ , which, in this case, magnifies the peaks at low energy and suppresses those at higher energy. The importance of  $D^{-1}$  is highlighted by again considering  $N(\omega)$ : we would expect large Kerr angle values at higher energy (around 6 eV). However, the corresponding peaks are suppressed by the  $D^{-1}$  factor. Hence, we are ready to conclude that the large Kerr peak at low energy has an “optical” origin; the features at high energy have an MO origin (they follow the trend of the numerator) but they do not result in large peaks due to the damped behavior of  $D^{-1}$  in this same energy range. This confirms in a more transparent and direct way what was already observed in Ref. [30] More important, the similar trend of  $D_0(\omega)$  ( $D$ ) and  $R\sigma_{xx}$  suggests that the presence of minima in the  $R\sigma_{xx}$  spectra may give rise to strong Kerr angles in the same energy range. On the other hand,  $R\sigma_{xx}$  is directly linked to the optical transitions, that is to details of the electronic structure of the materials: this could have far reaching consequences in *magneto-optical Kerr effect engineering*, provided that the electronic structure of the material can be tuned correctly in such a way as to *enhance* the features of the  $\text{Re } \sigma_{xx}$  minima.

## VII. CONCLUSION

We presented results of first-principles calculations of the magneto-optical properties of (Ga,Mn)As within density functional theory aimed at investigating in great detail the role of the electronic and magnetic properties in determining the magnetooptical behaviour of the material. The spectral features of the optical tensor in the 0-10 eV energy range were analyzed in terms of the band structure and density of states and the role of the dipole matrix elements was highlighted in terms of Brillouin zone *dissection*.

We found that different types of interband transitions contribute in shaping the conductivity tensor. The dipole matrix elements play a key role greatly affecting the optical spectra in the low as well as high energy ranges. Brillouin zone *dissection* reveals that different regions in the Brillouin zone (not necessarily symmetry points or lines) can contribute very differently in shaping the conductivity tensor; we find that the most active region in the IBZ

is around the R point.

Moreover, since the Kerr rotation spectrum is a result of a complex entanglement of real and imaginary contributions, we presented a possible way to analyze the calculated Kerr spectra in terms of a real representation of the Kerr angle. To the best of our knowledge, this has not been used as an analysis tool in the past, although it is implicit in Eq. 5. Using this representation, we have clearly elucidated the origin of the features of the Kerr spectra and have highlighted the role of the minima of  $\text{Re } \sigma_{xx}$  which can *possibly* correlate with a large Kerr angle (in our case, at low energies). Nevertheless, the results given above support the conclusion that at present it is difficult to give simple rules for the occurrence of large spectral features at specific laser-light frequencies. Indeed, both spin-orbit and exchange splitting effects are *entangled* in  $N(\omega)$ , which determines the overall behavior of the Kerr spectra and eventually the strength of the Kerr features. No simple rules can be given to *disentangle* their effects on the absolute magnitude of the Kerr angle. On the other hand, we found that part of the Kerr spectrum (in our case, the low energy range) is very sensitive to the shape of  $\text{Re } \sigma_{xx}$ , which is very closely related to details of the band structure of the materials.

While it is obvious that without a precise knowledge of the material band structure it is not possible to make a priori predictions of the Kerr angle magnitude, it is also true that a proper tuning of the band structure would allow one to consequently tune the magnitude and location of spectral peaks through the  $D_0$  term, whose spectral behavior is very close to  $\text{Re } \sigma_{xx}$ . However, further studies are needed in order to better elucidate how this proper tuning of the underlying electronic structure can be achieved (i.e. by making use of alloying, pressure, strain field) in order to enhance the minima of  $\text{Re } \sigma_{xx}$ . Therefore, we expect that computational materials design can substantially contribute to *magneto-optical Kerr effect engineering* in the future.

## VIII. ACKNOWLEDGMENTS

One of the authors (A. Stroppa) thanks G. Kresse for useful comments and fruitful discussions; this work started during a stay at Dipartimento di Fisica Teorica, Università degli Studi di Trieste, Strada Costiera 11, I-34014 Trieste, Italy and INFN-CNR DEMOCRITOS National Simulation Center, Trieste, Italy.

Work at Northwestern University was supported by the United States NSF (through its MRSEC program at the Materials Research Center).

## APPENDIX

Here we give an explicit representation of the *complex* Kerr angle ( $\theta_k + i\eta_k$ , Eq. 5) in the form  $\alpha + i\beta$ , where  $\alpha$  and  $\beta$  are real functions: the Kerr angle ( $\theta_k$ ) corresponds to  $\alpha$ . To this end, we need to calculate the square root of the complex number in the denominator of Eq. 5. It can be helpful to make use of the following formula[72]: given  $\sqrt{a + ib} = p + iq$  we have

$$p = \frac{1}{\sqrt{2}} \sqrt{\sqrt{a^2 + b^2} + a} \quad q = \frac{\text{sgn}(b)}{\sqrt{2}} \sqrt{\sqrt{a^2 + b^2} - a} \quad (9)$$

where  $\text{sgn}(b)$  is the sign of  $b$ . In our case,

$$\sqrt{1 + \frac{4\pi i}{\omega} \sigma_{xx}} = \sqrt{(1 - \frac{4\pi}{\omega} I\sigma_{xx}) + i\frac{4\pi}{\omega} R\sigma_{xx}}$$

where R and I stand for real and imaginary part and  $a = 1 - \frac{4\pi}{\omega} I\sigma_{xx}$ ,  $b = \frac{4\pi}{\omega} R\sigma_{xx}$ . By definition,  $b$  is positive.

In order to get rid of the complex number in the denominator of Eq. 5, we multiply numerator and denominator by  $\sigma_{xx}^*(p - iq)$ . After some algebra, we express:

$$\theta_k + i\eta_k = -\frac{(Ap + Bq) + i(Bp - Aq)}{D_0 D_1} \quad (10)$$

Then the Kerr angle is:

$$\theta_k = -\frac{(Ap + Bq)}{D_0 D_1} \quad (11)$$

and the ellipticity is:

$$\eta_k = \frac{Aq - Bp}{D_0 D_1} \quad (12)$$

where  $A = R\sigma_{xy}R\sigma_{xx} + I\sigma_{xy}I\sigma_{xx}$ ,  $B = I\sigma_{xy}R\sigma_{xx} - R\sigma_{xy}I\sigma_{xx}$ ,  $D_0 = (R\sigma_{xx})^2 + (I\sigma_{xx})^2$  and  $D_1 = \sqrt{(1 - \frac{8\pi}{\omega})I\sigma_{xx} + \frac{16\pi^2}{\omega^2}D_0}$

In this representation, an explicit analytic relation for the Kerr spike can be derived using the Kramers-Kronig transformation: whenever the ellipticity vanishes, a spike in the Kerr spectra appears.[31] Thus, imposing that  $\eta_k = 0$ , we derive an analytic relation for  $\theta_k$  which

holds for the maximum or minimum in the Kerr spectra corresponding to zero ellipticity. From  $\eta_k = 0$ , we have either (a)  $A = \frac{Bp}{q}$  or (b)  $B = \frac{Aq}{p}$  and using Eq. 11 we obtain:

$$\theta_k = -A \frac{p^2 + q^2}{pD_0D_1} = -B \frac{p^2 + q^2}{qD_0D_1} \quad (13)$$

A necessary condition to produce a Kerr spike is that  $\frac{A}{B} = \frac{p}{q}$ .

- 
- [1] J. Kerr, *Philos. Mag.* **3**, 321 (1877).
  - [2] K. H. J. Buschow, P. G. van Engen, and R. Jongebreur, *J. Magn. Mater.* **38**, 1 (1983).
  - [3] M. Hartmann, B. A. J. Jacobs, and J. J. M. Braat, *Philips Tech. Rev.* **42**, 37 (1985).
  - [4] R. Waser, *Nanoelectronics and Information Technology: Advanced Electronic Materials and Novel Devices* (Wiley, Weinheim, 2003).
  - [5] C. D. Mee and E. D. Daniel, *Magnetic Recording* (McGraw-Hill, New York, 1987).
  - [6] M. Mansuripur, *The Physical Principles of Magneto-Optical Recording* (Cambridge University Press, New York, 1995).
  - [7] F. Schmidt, W. Rave, and A. Hubert, *IEEE Trans. Magn.* **21**, 1596 (1985); D. A. Herman, Jr., and B. E. Argyle, *IEEE Trans. Magn.* **22**, 772 (1986).
  - [8] R. Q. Wu and A. J. Freeman, *J. of Magn. Magn. Mat.* **200**, 498 (1999).
  - [9] S. D. Bader, E. R. Moog, and P. Grünberg, *J. Magn. Magn. Mater.* **53**, L295 (1986).
  - [10] W. Reim, O. E. Huesser, J. Schoenes, E. Kaldis, P. Wachter, and K. Seiler, *J. Appl. Phys.* **55**, 2155 (1984).
  - [11] J. L. Erskine and E. A. Stern, *Phys. Rev. B* **8**, 1239 (1973).
  - [12] W. Reim and P. Wachter, *Phys. Rev. Lett.* **55**, 871 (1985).
  - [13] H. Ohno, *Science* **281**, 51 (1998), and references therein.
  - [14] Y. Ohno, D. K. Young, B. Beschoten, F. Matsukura, H. Ohno, and D. D. Awschalom, *Nature (London)*, **402**, 790 (1999).
  - [15] H. Ohno, D. Chiba, F. Matsukura, T. Omiya, E. Abe, T. Dietl, Y. Ohno, and K. Ohtani, *Nature (London)*, **408**, 944 (2000).
  - [16] H. Ohno, H. Munekata, T. Penney, S. von Molnár, and L. L. Chang, *Phys. Rev. Lett.* **68**, 2664 (1992).

- [17] H. Munekata, H. Ohno, S. von Molnar, A. Segmüller, L. L. Chang, and L. Esaki, Phys. Rev. Lett. **63**, 1849 (1989).
- [18] H. Ohno, A. Shen, F. Matsukura, A. Oiwa, A. Endo, S. Katsumoto, and Y. Iye, Appl. Phys. Lett. **69**, 363 (1996).
- [19] J. A. Gaj, R. R. Galazka, M. Nawrocki, Solid State Commun., **25**, 193 (1978).
- [20] A. E. Turner, R. L. Gunshor, S. Datta, Appl. Opt., **22**, 3152 (1983).
- [21] K. Onodera, T. Masumoto, M. Kimura, Electron. Lett., **30**, 1954 (1994).
- [22] S. Sugano and N. Kojima, *Magneto-Optics* (Berlin, Springer-Verlag, 2000).
- [23] S. Sanvito, G. J. Theurich, and N. A. Hill, J. Supercond. **15**, 85 (2002).
- [24] G. Bouzerar, J. Kudrnovsky', L. Bergqvist, P. Bruno, Phys. Rev. B **68**, 081203 (R) (2003).
- [25] P. Mahadevan, A. Zunger, Phys. Rev. B **68** 075202 (2003).
- [26] M. van Schilfgaarde and O. N. Mryasov, Phys. Rev. B **63** 233205 (2001).
- [27] L. Bergqvist, P. A. Korzhavyi, B. Sanyal, S. Mirbt, I. A. Abrikosov, L. Nordström, E. A. Smirnova, P. Mohn, P. Svedlindh, and O. Eriksson, Phys. Rev. B **67** 205201 (2003).
- [28] L. M. Sandratskii, P. Bruno and J. Kudrnovsky', Phys. Rev. B **69**, 195203 (2004).
- [29] A. B. Shick, J. Kudrnovsky, and V. Drchal, Phys. Rev. B **69**, 125207 (2004).
- [30] S. Picozzi, A. Continenza, M. Kim, A. J. Freeman, Phys. Rev. B **73**, 235207 (2006).
- [31] H. Weng, Y. Kawazoe, and J. Dong, Phys. Rev. B, **74**, 85205 (2006).
- [32] H. Weng, J. Dong, T. Fukumura, M. Kawasaki, and Y. Kawazoe, Phys. Rev. B, **74**, 115201 (2006).
- [33] E. Wimmer, H. Krakauer, M. Weinert and A. J. Freeman, Phys. Rev. B **24**, 864 (1981); H.J. F.Jansen and A. J. Freeman, Phys. Rev. B **30**,561 (1984).
- [34] L. Hedin and B. I. Lundqvist, J. Phys. C4, 2064 (1971).
- [35] H. R. Hulme, Proc. R. Soc. (London) Ser. A **135**, 237 (1932).
- [36] C. Kittel, Phys. Rev. **83**, A208 (1951).
- [37] R. Kubo, J. Phys. Soc. Japan **12**, 570 (1957).
- [38] C. S. Wang and J. Callaway, Phys. Rev. B **9**, 4897 (1974).
- [39] M. Singh, C. S. Wang, and J. Callaway, Phys. Rev. B **11**, 287 (1975).
- [40] P. Drude, Phys. Z. **1** , 161 (1900).
- [41] A. Sommerfeld and H. Bethe, *Handbuch der Physik* (Springer-Verlag, Berlin, 1933).
- [42] A. P. Lenham and D. M. Treherne, in *Optical and Electronic Structure of Metals and Alloys*,

- edited by F. Abels (North-Holland, Amsterdam, 1966).
- [43] V. Antonov, B. Harmon and A. Yaresko, *Electronic Structure and Magneto-Optical Properties of Solids* (Kluwer Academic, Dordrecht, 2004).
  - [44] R. P. Feynman, Phys. Rev. **56**, 340 (1939).
  - [45] H. J. Monkhorst and J. D. Pack, Phys. Rev. B **13**, 5188 (1976).
  - [46] M. Jain, L. Kronik, J. R. Chelikowsky, V. V. Godlevsky, Phys. Rev. B **64**, 245205 (2001).
  - [47] B. Sanyal and S. Mirbt, Journal of Magnetism and Magnetic Materials **290-291**, 1408 (2005).
  - [48] E. Kulatov, H. Nakayama, H. Mariette, H. Ohta, and Y. A. Uspenskii Phys. Rev. B **66**, 045203 (2002).
  - [49] H. Katayama-Yoshida and K. Sato, Physica B **327**, 337 (2003).
  - [50] Y. J. Zhao, W. T. Geng, K. T. Park, and A. J. Freeman, Phys. Rev. B **64**, 35207 (2001).
  - [51] M. Jain, L. Kronik, J. R. Chelikowsky, and V. V. Godlevsky, Phys. Rev. **64**, 245205 (2001).
  - [52] S. H. Wei, X. G. Gong, G. M. Dalpian and S. H. Wei, Phys. Rev. B **71**, 144409 (2005).
  - [53] R. Wu, Phys. Rev. Lett. **94**, 207201 (2005).
  - [54] H. Ebert, Rep. Prog. Phys. **59**, 1665 (1996).
  - [55] P. N. Argyres, Phys. Rev. **97**, 334 (1955).
  - [56] J. L. Erskine, E. A. Stern, Phys. Rev. B **8**, 1239 (1973).
  - [57] M. Singh, C. S. Wang, and J. Callaway, Phys. Rev. B **11**, 287 (1975).
  - [58] In this framework, accidental degeneracy corresponds to an almost equal energy level for the spin-up and spin-down states, *i.e.* a crossing of spin-up and spin-down curves at some  $k$ -point in Fig. 2. The inclusion of spin-orbit coupling may lead to a *repulsion* of the crossing majority and minority bands. On the other hand, systematic degeneracy corresponds to the usual degeneracy imposed by all the transformations of the spatial symmetry group.
  - [59] B. R. Watts, J. Phys. C: Solid State. Phys. **6**, 3605 (1973).
  - [60] G. B. Shaw, J. Phys. A.: Math., Nucl. Gen., **7**, 1537 (1974).
  - [61] W. A. Harrison, Phys. Rev. **147**, 467 (1966)
  - [62] H. Ehrenreich, H. R. Philip, and B. Segall, Phys. Rev. **132**, 1918 (1963).
  - [63] Spin-flip transitions are allowed within the electric dipole approximation when spin-orbit coupling is included, but are omitted in our work since their effect is negligible.
  - [64] D. K. Misemer, J. Magn. Magn. Mater. **12**, 267 (1988).
  - [65] E. J. Singley, R. Kawakami, D. D. Awschalom and D. N. Basov, Phs. Rev. Lett. **89**, 097203

- (2002); E. J. Singley, K. S. Burch, R. Kawakami, J. Stephens, D. D. Awschalom and D. N. Basov, Phys. Rev. B **68**, 165204 (2003).
- [66] K. S. Burch, J. Stephens, R. K. Kawakami, D. D. Awschalom, and D. N. Basov, Phys. Rev. B **70**, 205208 (2004).
- [67] E. Kojima, R. Shimano, Y. Hashimoto, S. Katsumoto, Y. Iye, and M. Kuwata-Gonokami, Phys. Rev. B **68**, 193203 (2003).
- [68] E. M. Hankiewicz, T. Jungwirth, T. Dietl, C. Timm and J. Sinova, Phys. Rev. **70**, 245211 (2004).
- [69] The dielectric constant and conductivity enter into a determination of the optical properties of a solid in the combination:  $\varepsilon_{\alpha\beta}(\omega) = \delta_{\alpha\beta} + \frac{4\pi i}{\omega} \sigma_{\alpha\beta}(\omega)$ .
- [70] J. Y. Rhee, B. N. Harmon and D. W. Lynch, Phys. Rev. B **55**, 4124 (1997).
- [71] J. Schoenes and W. Reim, Phys. Rev. Lett. **60**, 1988 (1988).
- [72] S. Rabinowitz, Mathematics and Informatics Quarterly, **3**, 54 (1993).



FIG. 1: Total and atomic- angular momentum- projected density of states (DOS) in  $\text{Ga}_{.75}\text{Mn}_{.25}\text{As}$ . Positive and negative curves refer to spin-up and spin-down components, respectively. The Fermi level is fixed at zero energy.

FIG. 2: (Color on line) Spin-polarized band structure for  $\text{Ga}_{.75}\text{Mn}_{.25}\text{GAs}$  along the symmetry lines  $\Gamma$ -X-M- $\Gamma$ -R-M in the irreducible BZ plotted without spin-orbit interaction for clarity: parts (a) and (b) refer to spin-up (-down), respectively. The horizontal line marks the Fermi level (zero energy). Numbers in round brackets at  $\Gamma$  label groups of bands discussed in the text. The vertical lines indicate the different possible band to band transitions at 0.4, 1.1, 2.8, 3.8 eV within 0.1 eV (solid black, dotted blue, dashed red and dot-dashed orange respectively). The labels for symmetry points and lines are according to the standard group-theoretical notation of Bouckaert, Smoluchowski, and Wigner. Spin-orbit effects are neglected.

FIG. 3: Calculated real (a) and imaginary (b) parts of diagonal and off-diagonal components of the optical conductivity. The Drude term has not been included in the spectra. Vertical lines in  $\text{Re } \sigma_{xx}$  indicate features discussed in the text.

FIG. 4: Selected contributions from spin-up (solid line) and spin-down (dashed line) transitions to the total  $\text{Re } \sigma_{xx}$  spectra. The joint density of states (JDOS) is also reported, in arbitrary units.

FIG. 5: (a) Real part of the diagonal conductivity: our calculated spectrum (bold line) is compared with the results of model calculations (dashed line) from Ref.[68] and experiments (dotted line) from Ref.[65]. The inset in panel (a) shows the difference between the interband and the total (interband + intraband) conductivity. Panels (b) and (c) show the calculated real and imaginary parts of the dielectric constant, respectively, with (bold line) and without (dashed line)  $\lambda$  fitting. Ellipsometry results from Ref.[66] are also shown (solid line).

FIG. 6: Prospective view of the irreducible wedge of Brillouin zone showing the origin of the interband transitions at  $\sim 3.8$  eV. The length of the arrows shows the relative contributions to  $\text{Re } \sigma_{xx}$  in the energy interval 3.6-4.0 eV (see Fig. 3). Increasing of the length of the arrows represents an increasing contribution. See text for further details.

FIG. 7: (Color online) (a) Ellipticity and Kerr angle; the main features of the Kerr spectra are indicated by arrows; (b) Different contributions to the numerator of the formula presented in Sect. VI and the Appendix (arrows indicate the main spectral features); (c,d,e) decomposition of the denominator (see text for details). Arbitrary units are used except for the Kerr angle (in decimal degree). See text for details.

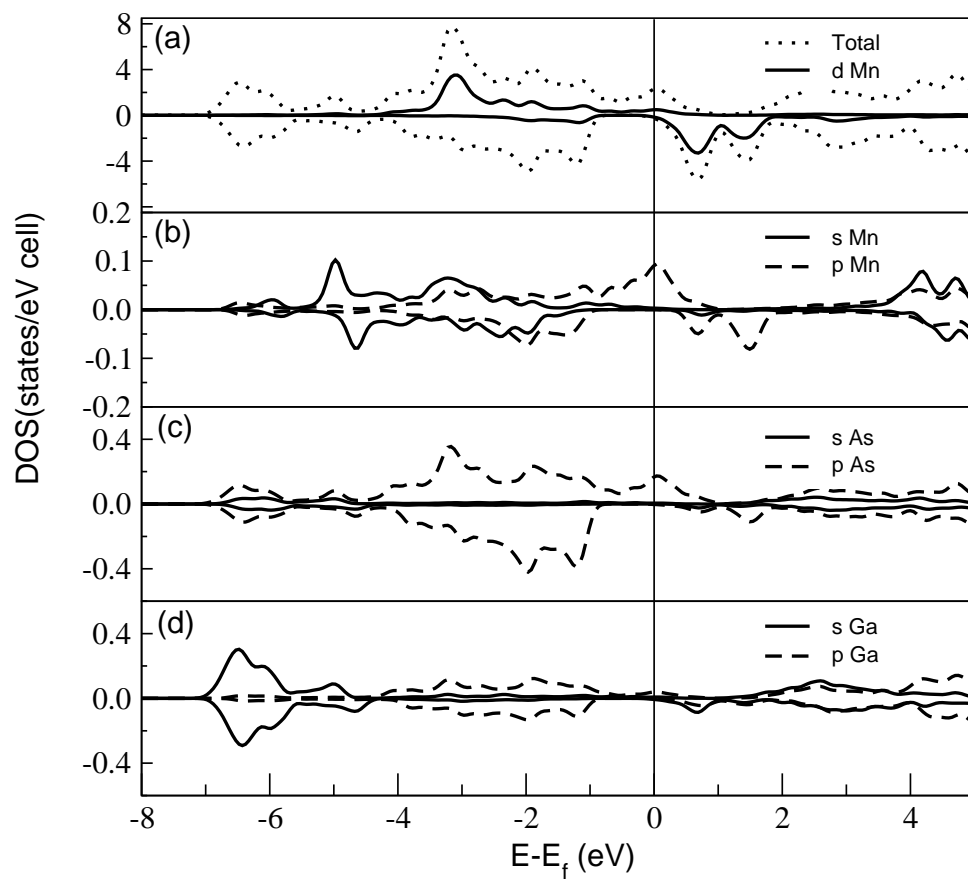


Fig. 1

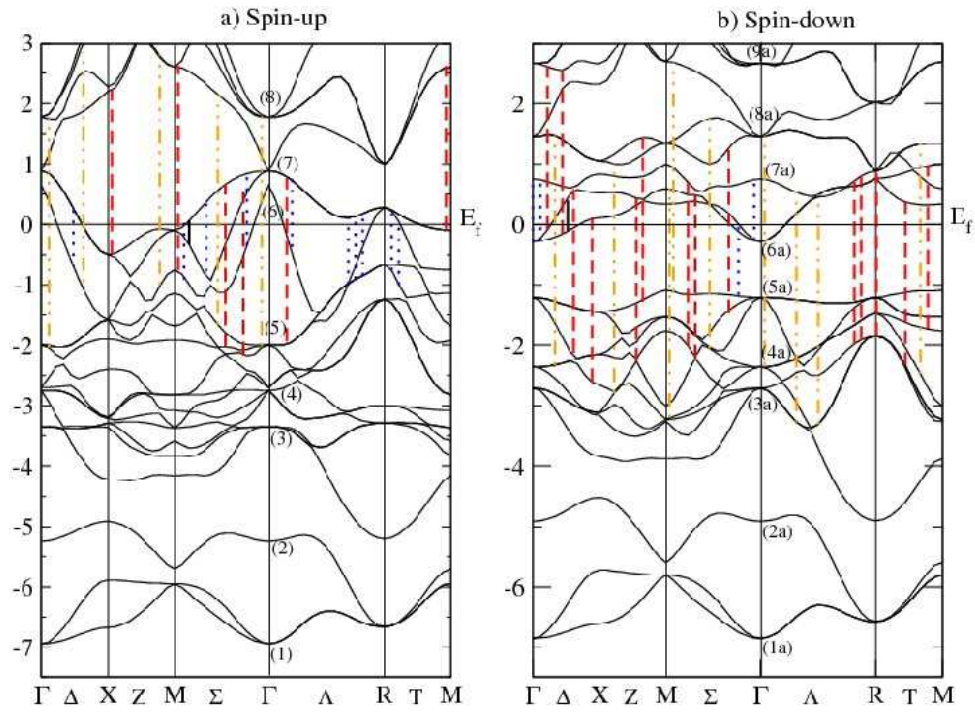


Fig. 2

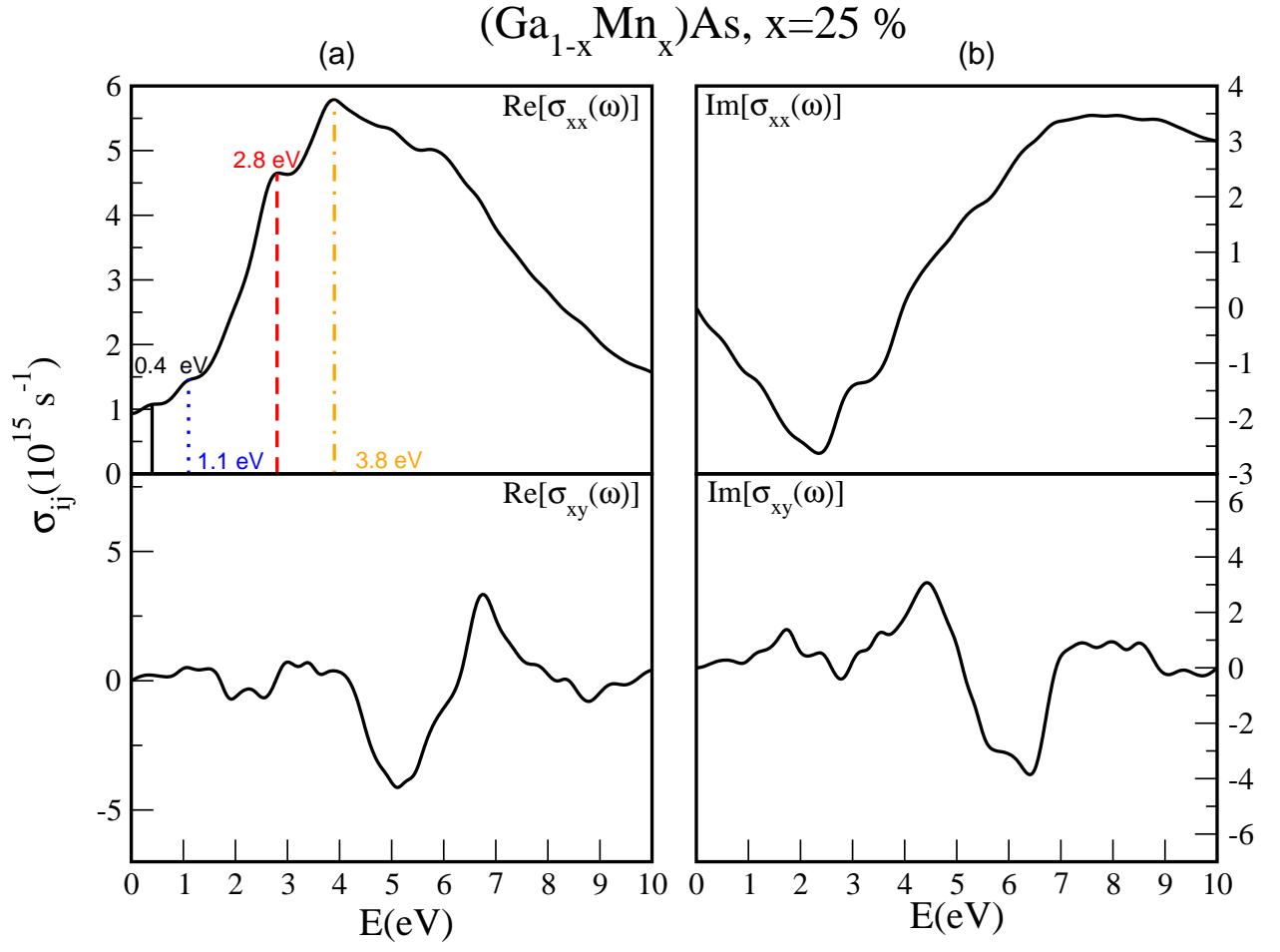


Fig. 3

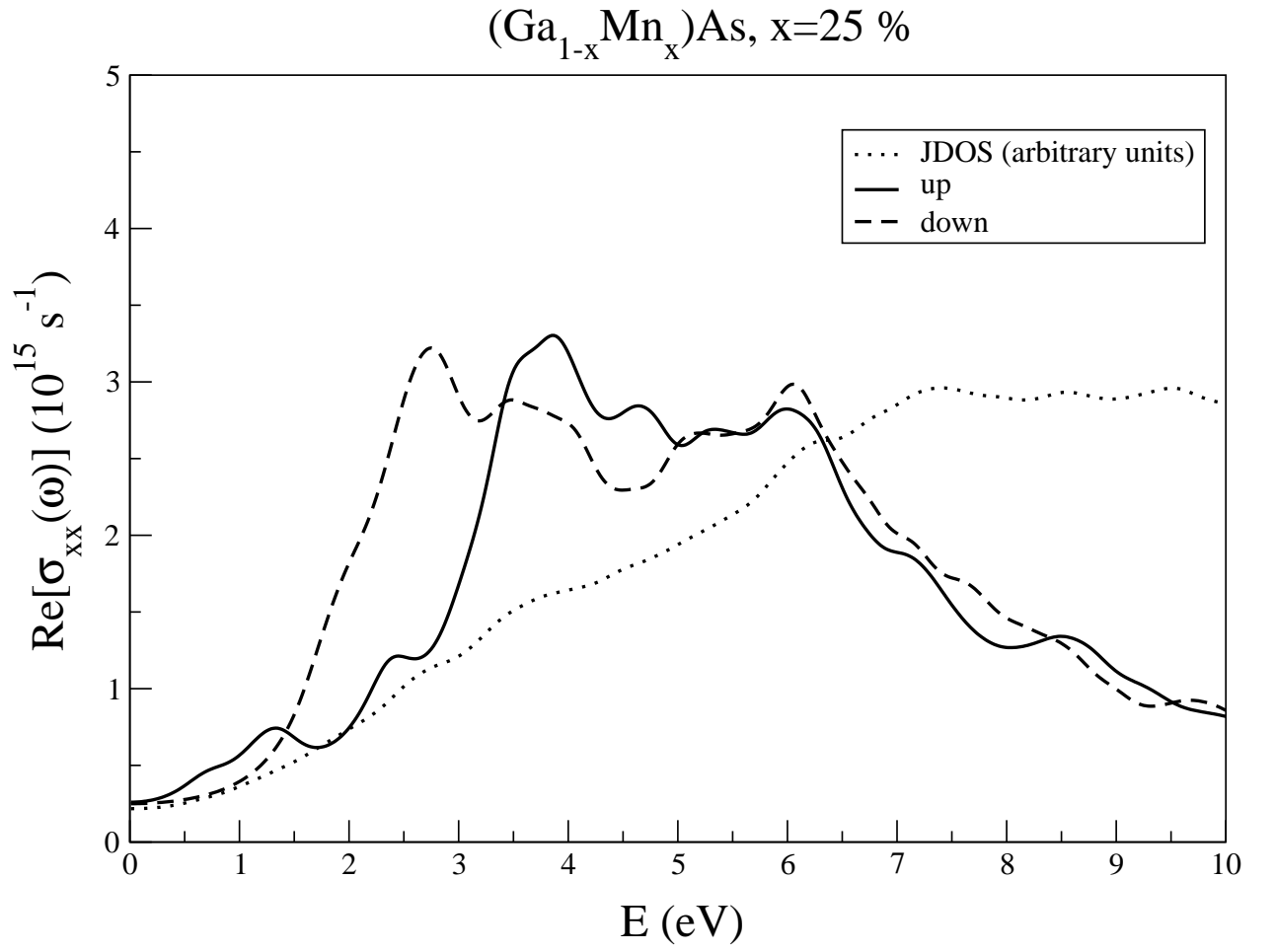


Fig. 4

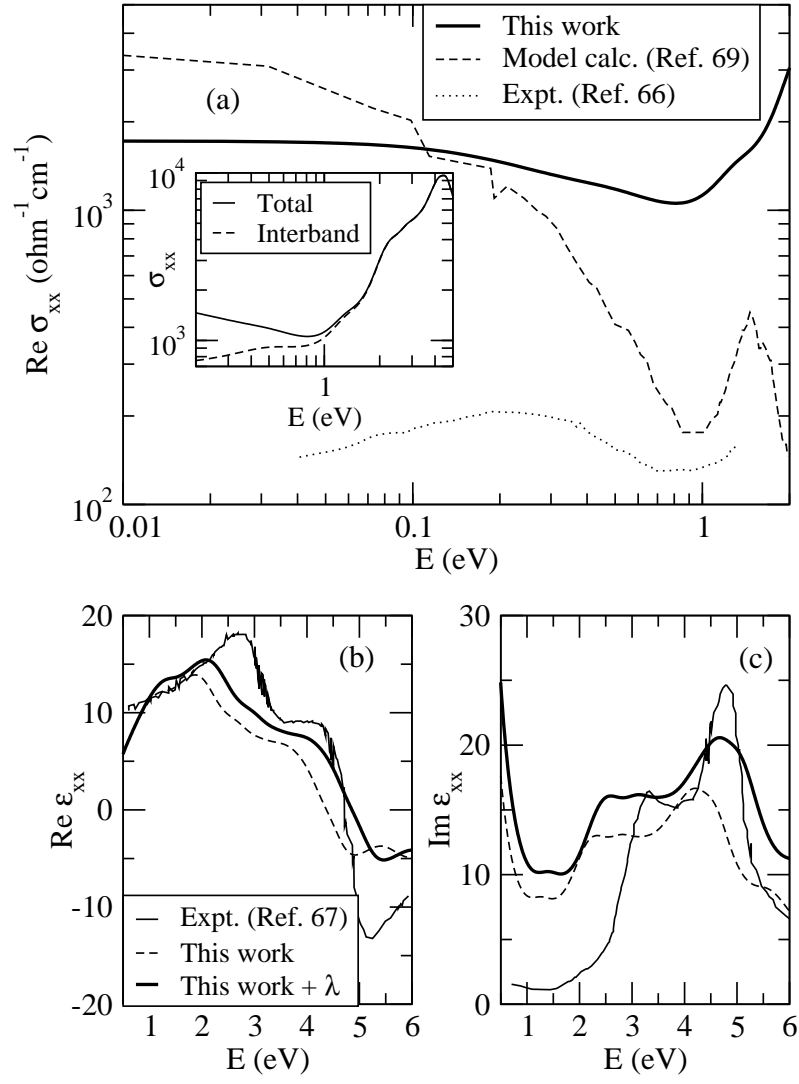


Fig. 5

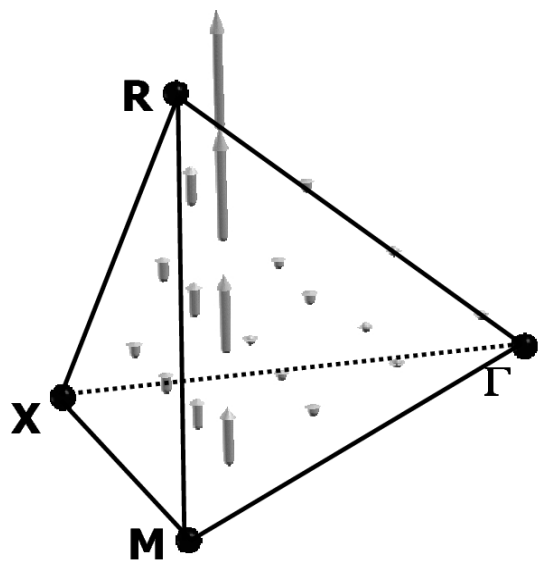


Fig. 6



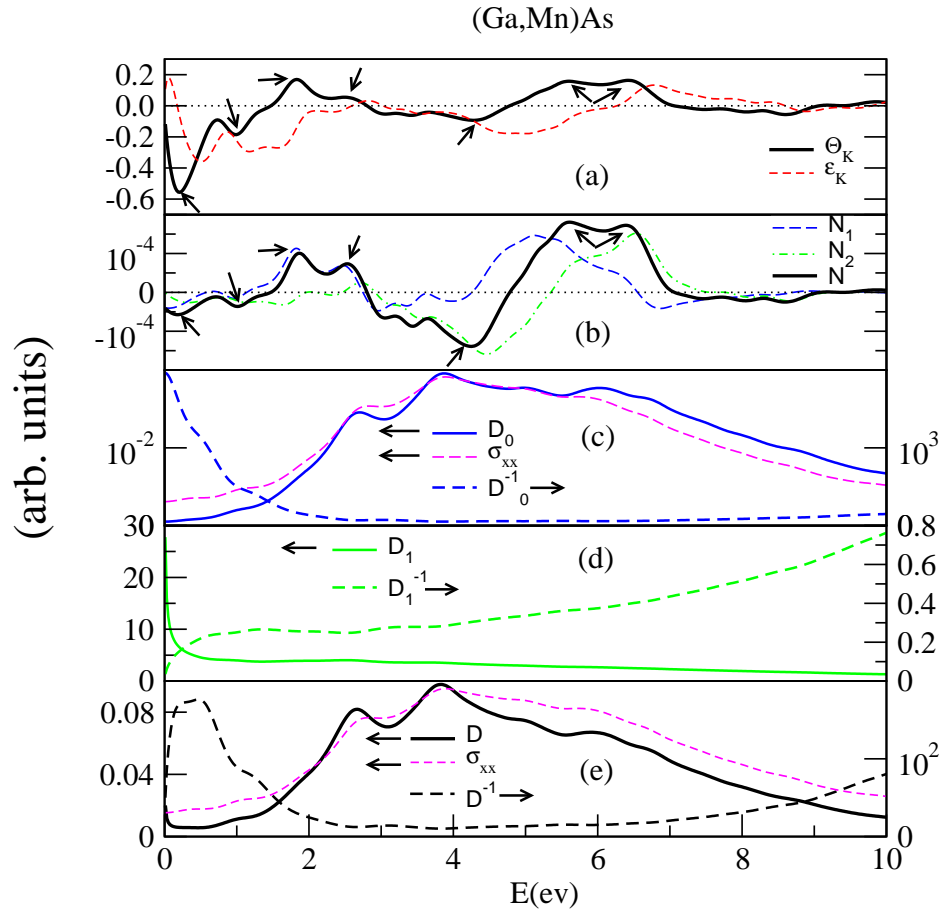


Fig. 7